Soft Matter

Accepted Manuscript

This is an *Accepted Manuscript*, which has been through the Royal Society of Chemistry peer review process and has been accepted for publication.

Accepted Manuscripts are published online shortly after acceptance, before technical editing, formatting and proof reading. Using this free service, authors can make their results available to the community, in citable form, before we publish the edited article. We will replace this *Accepted Manuscript* with the edited and formatted *Advance Article* as soon as it is available.

You can find more information about *Accepted Manuscripts* in the Information for Authors.

Please note that technical editing may introduce minor changes to the text and/or graphics, which may alter content. The journal's standard Terms & Conditions and the Ethical guidelines still apply. In no event shall the Royal Society of Chemistry be held responsible for any errors or omissions in this *Accepted Manuscript* or any consequences arising from the use of any information it contains.

ROYAL SOCIETY OF CHEMISTRY

www.rsc.org/softmatter

TOC

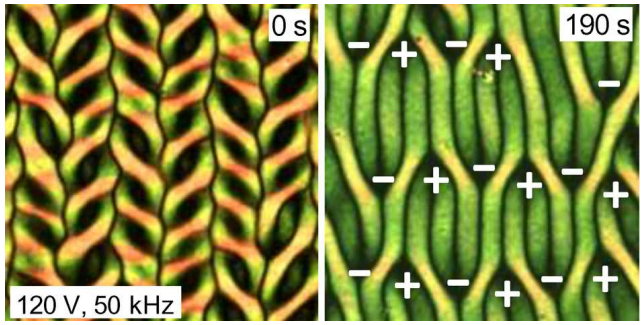

Metastable chevrons formed of edge dislocations in the inplane normal roll electroconvective state (left) relaxing exponentially into the quasi-steady state (right).

Cite this: DOI: 10.1039/c0xx00000x

www.rsc.org/xxxxxx

PAPER

Dislocations and metastable chevrons in the electroconvective inplane normal roll state of a bent core nematic liquid crystal

Kanakapura S. Krishnamurthy,*[a] Pramod Tadapatri,[b] and P. Viswanath[a]

Received (in XXX, XXX) Xth XXXXXXXXX 20XX, Accepted Xth XXXXXXXXX 20XX

DOI: 10.1039/b000000x

We report experimental results on the formation, dynamics and annihilation of edge dislocations of opposite topological charge in the electroconvective inplane vortex state of a bent-core nematic liquid crystal. The approach of paired oppositely charged defects toward each other is a two step process. Near constant velocity at large separation and accelerated motion close to annihilation are found, as in the case of nematic rolls belonging to standard electroconvection. Periodic arrays of dislocations of alternating polarity form upon a sudden, strong elevation of the control parameter. Chevron structures that appear between undulatory defect chains are metastable and their decay with time is accompanied by an exponential reduction in the dislocation density. The initial periodicity of defect chains also drops exponentially with increasing field.

1 Introduction

In classic anisotropic electroconvection of nematic liquid crystals, chevrons are a herringbone-like roll structure formed in either the conduction or the dielectric regime.[1-3] Structurally, chevrons are non-unique in that they exhibit varied morphologies depending on the sample configuration, material properties and field parameters. For example, the so-called dielectric chevrons form in a planar monodomain of a nematic liquid crystal with negative permittivity anisotropy $\varepsilon_a = \varepsilon_{\|} - \varepsilon_{\perp}$ and positive conductivity anisotropy $\sigma_a = \sigma_{\|} - \sigma_{\perp}$ ($\|$ and $\perp$ denoting the direction relative to the nematic director **n**), in the dielectric regime of quasistationary space charges and oscillating director field; this regime occurs above the cut-off frequency f_c of the conduction regime, wherein the charges follow the field while the director pattern is nearly static.[4-12] In the course of the evolution of these chevrons, the fluid breaks up first, at a critical field E_c, into very narrowly spaced dielectric rolls with the wave vector **q** along the initial director $\mathbf{n}_0$; above E_c, edge dislocations of opposite topological charge nucleate, their density increasing with the field strength; eventually, the defects become spatially correlated so as to form periodic chains normal to the easy axis, with the defect-sign alternating from one chain to the next. As a topological necessity, the rolls then rotate about the layer normal, alternately clockwise and anticlockwise between the chains, while the director concomitantly twists around to remain nearly parallel to the local wave vector. This evolution of the dielectric chevron texture is likened to the development of Turing patterns in reaction-diffusion systems.[8,9] Chevrons of a different kind form in planarly aligned very high conductivity nematics at very high frequencies.[13,14] They are conjectured to be a result of the coupling between the inertia mode manifesting optically as broad domains and either the linear dielectric roll instability or the Williams roll instability of the conduction regime. In the first case, we have narrowly spaced (thin) chevrons and, in the second, relatively wider (thick) chevrons. The chevron instability is also obtained in initially homeotropic high conductivity nematics in the conduction regime, far above the threshold of the Freedericksz transition.[15-17] In this case, they are termed defect-mediated chevrons or defect-free chevrons depending on their structure which, in turn, is determined by the bifurcation sequence to which they belong: Below a well defined frequency f_w, the sequence is Freedericksz transition→normal rolls→abnormal rolls →defect chaos→defect-mediated chevrons; above f_w, it is Freedericksz transition→ prewavy mode→ defect-free chevrons. The prewavy and broad domain modes are structurally very similar, involving periodic modulations of the inplane or **c**-director; however, the latter is an anisotropic instability, while the former is reported to display the threshold features of the isotropic (electrolytic) mode.[17] Defect mediated chevrons have also been reported for a nematic composed of banana like dimeric molecules and having a short range smectic order.[18]

The various electroconvective chevron states discovered thus far are all exhibited by straight-core or calamitic nematogens. The reported electroconvection phase diagrams of bent-core nematics[19-25] do not show any chevron instability, although chevrons have been reported beyond the dielectric inversion frequency for a bent-rod nematic liquid crystal.[26] This paper concerns the transient chevron instability induced in bent core nematics by a sudden, large jump in the control parameter $\Sigma = (U^2/U_c^2) - 1$, U and U_c being the applied and threshold voltages respectively. Indeed, such an instability was first observed in a bent core compound by Wiant et al.,[19] who described it as the 'knitting' instability, but did not recognize it as constituted of

chevrons. Our interest in this instability was aroused by its metastable character and spontaneous relaxation into a stable non-chevron state dominated by defects. We studied this relaxation in detail to learn of the dynamics of chevron decay. The situation here is somewhat similar to that of phase ordering through defect coarsening in quenched systems of lowered symmetry. [27] In previous dynamical scaling investigations of this latter type, the topological defects considered are mostly singular and nonsingular disclination lines (strings). Chevrons, on the other hand, involve edge dislocations self-organizing into a 2-D vortex lattice. Their decay would therefore constitute a new phenomenon that we intend to describe and discuss here. In this process, we also deal with the distinguishing properties of dislocations in anisotropic roll systems in which the stream lines are confined to the layer plane. It may be noted that the nematic convective rolls studied hitherto for their structural defects[28-38] are of the conventional type with the axes of flow, rather than the flowlines, in the layer plane.

2 Experimental section

The material studied, 4-cyanoresorcinol bis[4-(4-n-nonyloxybenzoyloxy)benzoate] (9CN), shows the phase sequence

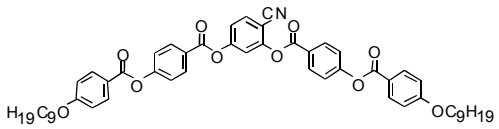

Cr 92 °C *N* 125.6 °C *I*, with *Cr*, *N* and *I* denoting respectively the crystal, nematic and isotropic phases. The *N* phase supercools to as low as 64 °C before undergoing a monotropic transition to an unidentified (presumably columnar) mesophase *X* exhibiting spherulitic aggregation. On further cooling, transition to the crystal occurs at about 40 °C. The static dielectric anisotropy of nematic 9CN is negative below 122.2 °C, but reverses sign above this temperature.[22] At 80 °C at which the present studies were carried out, the anisotropy is about –2.4. The sample cells were sandwich type, constructed of passivated indium tin oxide (ITO) coated glass plates from Delta Technologies. The planar alignment was secured by spin coating the ITO electrodes with polyimide and then buffing unidirectionally the coated surfaces on a velvet cloth. Mylar spacers, heat-sealed to the electrodes through cooling from 250 °C under a uniform pressure, determined the cell gap d, measured interferometrically. For optical observations, a Carl-Zeiss Axio Imager.M1m polarizing microscope equipped with an AxioCam MRc5 digital camera was used. The sample temperature T was maintained to an accuracy of ±0.1 °C by an Instec HCS402 hot-stage connected to a STC200 temperature controller. The voltage source was a Stanford Research Systems DS345 function generator coupled to a FLC Electronics voltage amplifier (model A800). The cited rms values of the applied voltage $U(t)=\sqrt{2}\,U_{\rm rms}\sin\omega t$ were measured with a Keithley-2002 multimeter. For reference, we employ a rectangular frame xyz, and take the initial director $\mathbf{n_o}=(1,0,0)$ and the applied field $\mathbf{E}=[0,0,\,U(t)/d]$. In the description of patterns, we indicate the setting of the polarizer P and analyzer A by P(β)-A(β'), where β and β' are the angles in degrees made by the corresponding transmission axes with the x direction.

3 Results and discussion

3.1 Dislocations in the inplane normal roll structure

In a previous report,[22] we have described the various temperature-determined scenarios of bifurcation observed in a layer of planar nematic 9CN driven by an ac field. For our present purpose, it is sufficient to consider the schematic phase diagram in Fig. 1 corresponding to 80 °C. It shows two electroconvective states, namely the inplane longitudinal roll (ILR) state and the inplane normal roll (INR) state, separated by the frequency of transition $f_{\rm LN}$. Here the term 'inplane' refers to the flow field, implying that the plane of the vortices is the layer plane xy; and the terms 'longitudinal' and 'transverse' refer to the direction along which the rolls are extended in the layer plane (or the disposition of stripes/domains in planform) relative to the initial alignment direction $\mathbf{n_o}$. The director modulation at threshold U_c is primarily azimuthal for both ILRs and INRs. In particular, for the INRs with which this study is exclusively concerned, the azimuthal deviation φ may be expressed as $\varphi=\varphi_o \sin qx \sin(\pi z/d)$, where q is the angular wave number. In other words, at threshold, the INR structure possesses translational symmetry, being repetitive along $\mathbf{n_o}$, with the roll-periodicity $\lambda_N=2\pi/q$ equal to the separation between alternate rolls having the same sense of fluid rotation. Optically, under white light illumination, the rolls are best visualized in birefringence contrast as an array of coloured stripes parallel to y. With the polarizer along x and the analyzer slightly uncrossed, the adjacent bright bands appear differently coloured because of the opposite tilts in adjacent rolls, as depicted in the inset of Fig.1. At higher field strengths, the stripes are also revealed under shadowgraphic imaging, in either polarized or natural light, because of the periodic out-of-layer tilt θ becoming increasingly prominent.

As the constraint is slowly enhanced, the INR structure develops defects in periodicity at locations where two counter-rotating adjacent rolls originate or terminate. Such defects are associated with a pair of disclinations and are described as edge dislocations. They are analogous to the edge dislocations of the type $\Omega_a(\pi)+\Omega_a(-\pi)$ in the layered order of smectic A liquid crystals.[39] The topological charge Q associated with a dislocation

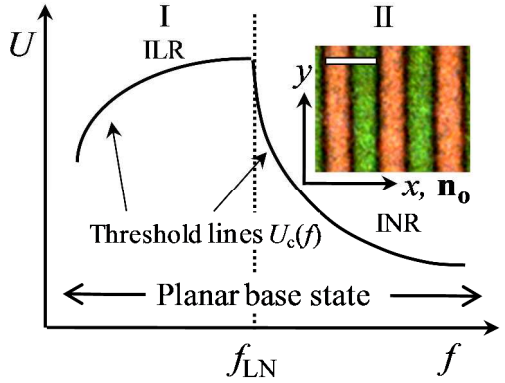

Fig. 1 Schematic of the primary bifurcation threshold U_c as a function of frequency f for nematic 9CN at 80 °C. ILR and INR denote 'inplane longitudinal roll' and 'inplane normal roll', respectively; $f_{\rm LN}\approx 10$ kHz is the transition frequency between the ILR and INR states, which are distinguished by their opposite $U_c(f)$ trends and orthogonal wave vectors. Inset: Optical texture in the INR state as observed between slightly uncrossed polarizers, P(0)-A(95), at f=50 kHz and 24.7 V (Σ=1.78). d=15.5 μm . Bar 40 μm.

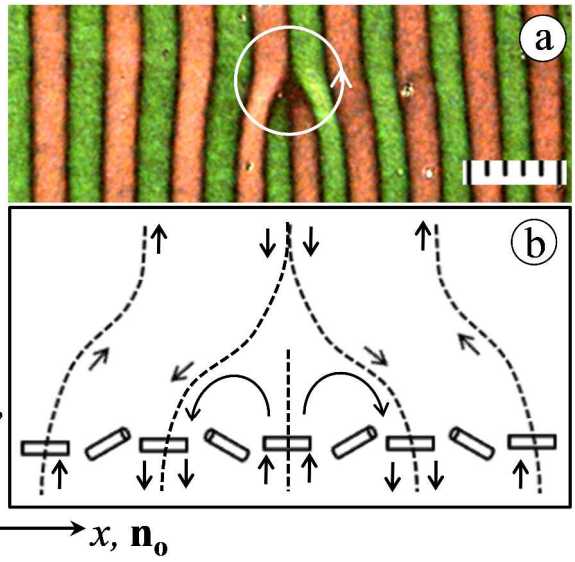

Fig. 2 (a) Photomicrograph of an edge dislocation formed in a sample of 9CN at T=80 °C. P(0)-A(95). f=50 kHz, Σ =3.03 and d=15.5 μm. 10 μm each scale div. (b) Schematic of an edge dislocation. The arrows indicate the streamlines corresponding to the experimentally observed tracer-particle trajectories. Cylinders represent the molecules with their inplane and out-of-plane deviations periodically modulated along x.

may be defined as

$$Q = \frac{1}{2\pi}\oint \mathbf{q}.\mathrm{d}\mathbf{s} = \pm 1, \qquad (1)$$

where **q**, the local wave vector normal to the stripe direction, is given by the local gradient of the phase variable, $\nabla\psi$; ψ is linear in x in the defect free periodic roll state. While computing the cyclic integral around a defect in the anticlockwise sense, the + sign applies to the dislocation at which an additional pair of domains terminates. We illustrate a positive dislocation in Fig. 2a. In Fig. 2b showing a schematic of this defect, the arrows indicate the streamlines corresponding to the experimentally observed tracer-particle trajectories and the cylinders represent the molecules with their inplane and out-of-plane periodic deviations along x.

3.2 Nucleation and motion of edge dislocations in the high field regime

The period of the normal roll pattern λ_N decreases considerably as the field is elevated, with the voltage variation of the wave number $\kappa = \lambda_N^{-1}$ being an s-shaped curve (see Fig. 14, Ref. 22). This narrowing of rolls comes about through the nucleation of ±1 edge dislocations occurring ever increasingly as the constraint is enhanced. In Fig. 3a-e, we illustrate the process of evolution and subsequent drifting apart of two paired dislocations in response to a stepwise field elevation. Here, by 'pairing' we mean that, of the two additional inplane rolls associated with each dislocation, one is common to the two dislocations. A comparison of panels (a) and (b) of Fig. 3 shows that the rolls, which are initially almost rectilinear along y, first become unstable against a long-wavelength undulatory perturbation under increased stress. This effect is analogous to the thermally induced layer undulation instability in the Smectic C phase[40] derived from the Smectic A phase. It is attributed to the tilting of the director away from the layer normal in the course of the phase transition; the resulting

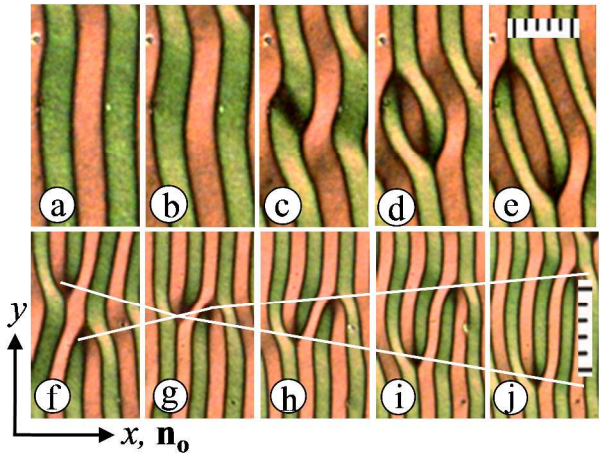

Fig. 3 (a-e) Generation and climbing motion of paired edge dislocations of opposite polarity; U= 44.7 V (Σ=8.1) in (a); 5 V increment between successive images; 5 μm each scale div. The period of about 30 μm in (a) reduces to about 20 μm in (e). (f-j) Field-induced climb of unpaired neighboring edge dislocations. U=54.5 V (Σ=12.6) in (f); 10 V increment between successive images; white lines through the corresponding dislocations indicate a decrease of climb rate with voltage beyond the crossover point in (g);10 μm each scale div. 50 kHz, 80 °C.

large dilatory stresses, in the absence of nucleation of new layers, lead to undulations. Here, under increased Σ, the enhanced average azimuthal tilt in a roll may be expected to lower the roll width and thereby enforce the rolls to develop, in the absence of nucleation of new rolls, undulations along their length (along y) in the layer plane. These undulations are eventually relaxed by the nucleation of edge dislocation pairs at higher voltages, as exemplified in Fig. 3c. With further Σ-increase, as illustrated in Fig. 3d and e, the positive and negative defects drift more and more along $+y$ and $-y$ directions, respectively, so that an overall increase in the wave number results.

When increasing the voltage in large steps, the dislocations climb to their new quasistatic positions in a very short time after each voltage switch and thereafter hardly display any conspicuous temporal instability. The climb of unpaired neighbouring dislocations of opposite polarity in response to U changing in increments of 5 V is shown in Fig. 3f-j. Here the

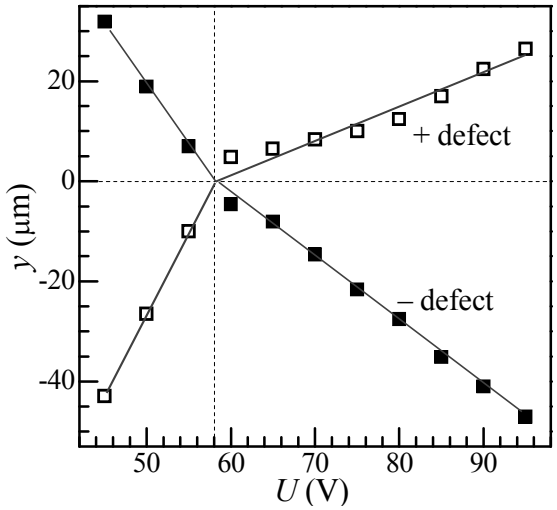

Fig. 4 Dependence of the y-displacement (climb) on voltage for two neighboring unpaired dislocations of opposite polarity. The crossover of the defects occurs for U≈58 V. 50 kHz. 80 °C.

voltage variation of displacement, for each of the defects, shows two sloping linear sections intersecting at the crossover point y=0. As further elaborated in Fig. 4, the rate $|dy/dU|$ of climb is considerably greater before the defects cross each other than afterwards; for the positive defect, the climb rate changes from 3.2 μm V^{-1} to 0.68 μm V^{-1} across the crossover point. Similarly, for the negative defect, the rate changes from 2.43 μm V^{-1} to 1.31 μm V^{-1}. There appears to exist between the dislocations a short range attraction force along y that contributes positively to the climb rate as long as the defects are approaching each other, but the effect turns negative when they are receding. This would explain the different displacement trends across the crossover voltage of about 58 V. Further, the voltage induced drift of a given dislocation is conditioned by the motion of various interacting dislocations around it and, not surprisingly, dy/dU may vary considerably for different local defect-environments. We found $|dy/dU|$ to range from almost 0 to 6 μm V^{-1} for different dislocations in the visual field. It is to be noted that the dislocations in Fig. 3f-j maintain a constant lateral separation of $\lambda/2$ for all voltages. In other words, the applied field does not induce a relative glide as that would lead to annihilation of defects and a decrease in the effective wave number.

While remaining in the high voltage regime, if Σ is suddenly lowered and then held constant, despite the presence of several defects in close proximity, some general dynamical trends associated with removal of roll pairs are noticed. We exemplify this in Fig. 5, where panels (a)-(e) belonging to a time series depict the process of annihilation of two paired dislocations, and panels (f)-(i), the coupled motion of 'bound' pairs. The former process involves two different forces, one leading to uniform motion for large defect separations and the other to accelerated motion before annihilation. This aspect is more systematically studied at smaller Σ values as will be seen in the next section. In

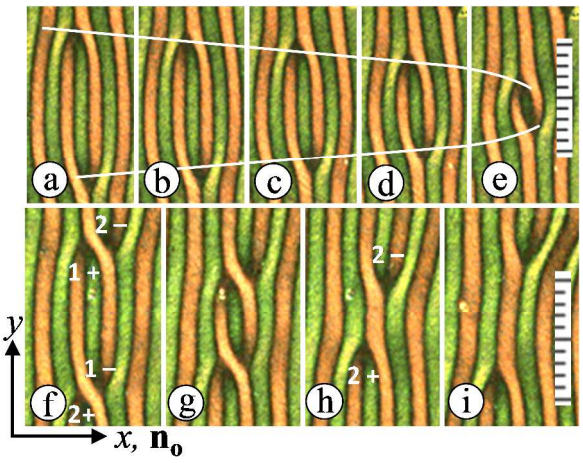

Fig. 5 (Color online) (a)-(e) Paired dislocations approaching each other toward eventual annihilation on reducing the control parameter from 5.1 to 3.9; the successive images are 12 minutes apart; 50 kHz, 80 °C; white lines through the images indicate the climb of dislocations as nearly uniform except close to annihilation, where it becomes accelerated. (f)-(i) Motion of 'paired' and 'bound' dislocations; defects 1+ and 1– are paired; further, 1+ is 'bound' to 2–, and 1– to 2+. The bound defects move together until the annihilation of (1+, 1–) pair; thereafter, the defects 2– and 2+ move in reversed directions; for (f)-(g) and (g)-(h), time interval is 15 minutes, and for (h)-(i), 30 minutes; 50 kHz, Σ=3.94, 80 °C. P(0)-A(95). 10 μm each scale div.

the case of bound pairs (Fig. 5f-i), as a rule, the paired dislocations (1±) annihilate first and then the unpaired defects (2±) separate increasingly. That the bound neighboring defects (1+, 2–), as also (1–, 2+), do not annihilate each other through glide is indicative of a stronger interaction between opposite defects when they are paired than when they are unpaired. It may also be due to a preference for climb over glide. Stability against glide has also been observed for edge dislocations in the structure of conventional electroconvection rolls formed at higher frequencies of the conduction regime.[30] From the correspondence between layered near equilibrium systems, such as the smectic A phase, and structures formed far-from-equilibrium, such as the convective rolls,[28,29] it is argued that the nature of deformation field around a dislocation is the key factor in the choice between climb and glide motions. Essentially, the strongly deformed region at a dislocation is separated from the less strained contiguous regions by a parabola with an aperture $\Pi=\sqrt{(k/B)}$, where k and B are the curvature elastic modulus and compression modulus, respectively. A large value of Π indicates preference for compression over curvature distortion and correspondingly the optimum configuration is approached through climb.

3.3 Dislocation dynamics in the low field regime

The motion of dislocations is a characteristic process by which the mismatch in the wave vector **q** is overcome. In a systematic study of the dynamics of edge dislocations, this mismatch is created in a controlled manner by employing the dependence of q on either of the electrical parameters f and U. For example, in the case of Williams rolls, the critical wave vector q_c and the critical voltage U_c corresponding to the fastest growing mode increase nonlinearly with f,[1-3] while q is practically independent of U (Fig. 6). Thus, the process of creating dislocations in the Williams roll structure relies usually on $q(f)$; typically, at a given f, Σ is increased sufficiently to generate many defect pairs; when all but a few of these pairs remain after relaxation into the stable state of wave number q_1, suddenly both f and Σ are lowered to their chosen values, thereby establishing a positive mismatch $\Delta q = q_1 - q_2$ with q_2 denoting the equilibrium or optimum wave vector in

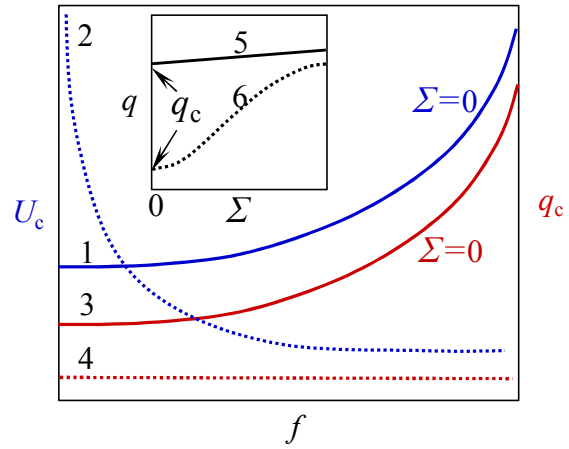

Fig. 6 Schematic of the frequency dependence of critical voltage U_c (lines 1, 2) and critical wave number q_c (lines 3, 4), with continuous lines for normal rolls of standard electroconvection and dotted lines for high frequency INR instability. Inset: Optimum wave number q as a function of control parameter Σ for the two instabilities.

the new situation.[32] It is important to note that q_1 remains unchanged with the jump in f and Σ as long as it is inside the stable band.[33] Pairwise annihilation of defects is then found to follow a regular dynamical trend: At large distances apart, the defects move with a constant velocity proportional to Δq and determined by the balance between dissipation and Peach-Koehler-like elastic force.[33] This velocity shows little dependence on the constraint. Prior to annihilation, within a range s^* that varies as $1/\Delta q$, the defects accelerate under mutual attraction. All these features observed in standard electroconvection have been explained using amplitude equations.[32,33] An analogous study for the INRs needs to rely on $q(U)$ rather than $q(f)$ since, significantly in this case, q_c is nearly independent of f, while $q(\Sigma)$ is an increasing function, as schematically shown in Fig. 6 (see also Ref. 22). Thus, in our present study on the motion of defects in the INR state, we first increased the control parameter to a value Σ_1 in the range 0.8-2.2, keeping f fixed at 50 kHz, thereby generating a large number of dislocations; after relaxation of most of the defects, a quasistable state with an effective wave number q_1 was reached. Then we decreased the control parameter to a value Σ_2 in the range 0.01-0.5. The optimisation of q under the lowered constraint was observed to occur in two distinct ways: (i) predominant climbing motion (along y) leading to eventual annihilation of paired defects, and (ii) initial climb followed by pre-annihilation glide (along x) of unpaired neighbouring defects of opposite polarity (which occurred rather infrequently and when the stripes were slightly inclined with respect to y). With each of these events, a roll-pair disappeared from the system and, when only a few dislocations were left in the visual field, we monitored their dynamics through time imaging. Fig. 7 gives typical plots of the separation s between paired defects as a function of time t for different values of Σ_2. The pattern in the visual field occupied an area of about $44d$ x $33d$, containing up to about 17 roll pairs or periods. While collecting the data shown in Fig. 7, it was ensured that only two opposite and paired dislocations existed in the visual field until their annihilation and the pattern was free of defects thereafter. Initially, if q_m and $q_o<q_m$ are the average wave numbers midway between the dislocations and in the outer regions, respectively, their average q_a may be assumed as the background wave number; if after the annihilation, the final wave number is q_f, $\Delta q=q_a-q_f$ then represents the wave number mismatch. As has been demonstrated previously for the dislocations in the Williams roll structure, analysis of shadowgraphic images based on complex demodulation method can provide accurate location of topological point defects.[32,33] We find that this technique is also suitable for the patterns recorded here using birefringence contrast. The roll pattern is represented by $\psi(x, y) = A(x, y)\exp(iqx)$ + c.c., where $A(x, y)$ signifies the complex amplitude field. We have adopted the complex demodulation method described in Ref. 33 to extract $A(x, y)$ from the roll pattern and to locate the defects after removal of the underlying periodicity. Briefly, the two dimensional image of the roll pattern is background subtracted and smoothened using a Gaussian filter (width 1). The processed image is Fourier transformed and the complex conjugate part of it is set to zero. The peak at q is extracted and shifted to origin after filtering the higher harmonics. This removes the underlying periodicity in the Fourier space. An

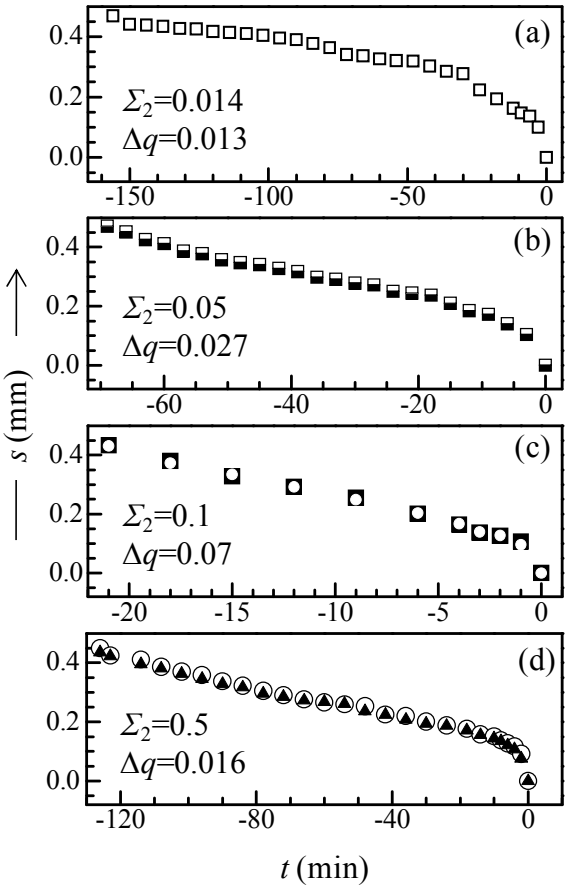

Fig. 7 Time dependence of the separation between two oppositely charged edge dislocations approaching each other toward eventual annihilation under constant control parameter Σ_2. The initial control parameter used for generating the defects is Σ_1=0.8 (a)-(c), and 2.16 (d). White circles in (c) and filled triangles in (d) are from image analysis using complex demodulation technique. Other data are from mechanical measurements.

inverse transform is applied to yield the complex amplitude field $A(x, y)$ in the real space. The intersection of real and imaginary parts of $A(x, y)$ gives the location of the defect core where the absolute value of $A(x, y)$ is zero and the phase is undefined. A customized code written in python exploiting the features of the module SciPy[41] is used for analyzing the time series of images. Fig. 8 shows an INR pattern with two paired dislocations in birefringence contrast and typical results of FFT analysis on such images. The distances from defect locations arrived at in this manner are shown in panels (c) and (d) of Fig. 8 that correspond to relatively large values of Σ. That the distances measured mechanically are in close agreement with those from the FFT analysis is clear from the superimposed data points in these panels. For lower values of Σ [(a) and (b) of Fig. 7], the pattern contrast was found too low for the complex demodulation technique to yield accurate results.

The process of annihilation revealed in Fig. 7 is understandably very slow because of the high viscosity in the supercooled nematic state at 80 °C. On repeating the experiment at 110 °C, we found the $s(t)$ profile to be no different, except for the annihilation time of about 2 minutes for the same conditions as in Fig. 7c. Characteristically, the $s(t)$ plot shows the defect motion to be broadly uniform except close to the annihilation

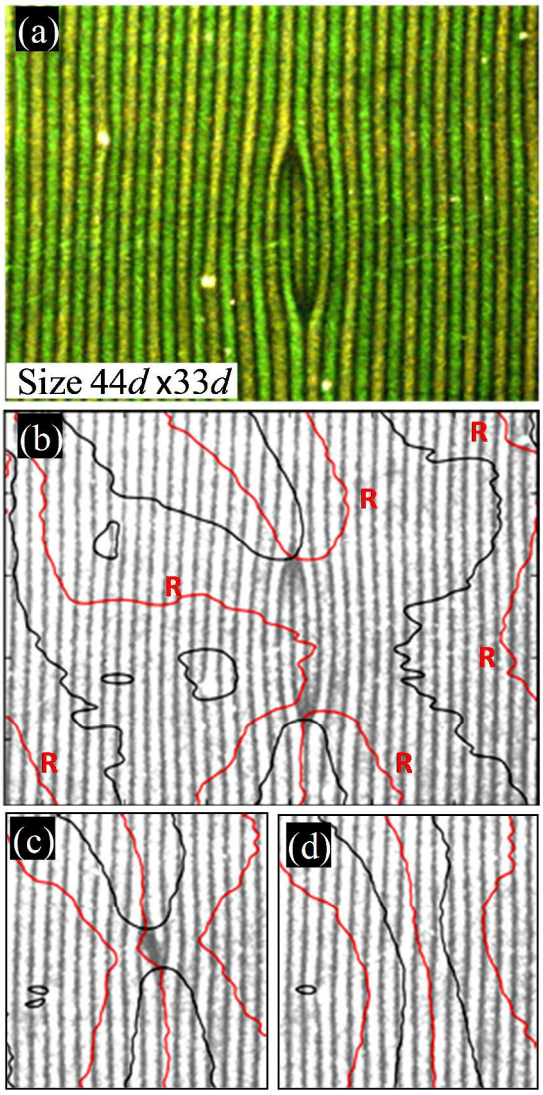

Fig. 8 (a) Micrograph of an INR pattern in birefringence contrast [P(0)–A(100)] showing two paired, opposite dislocations. (b) Plot of Im[$A(x, y)$]=0 (black lines) and Re[$A(x, y)$]=0 (red lines marked R) for the pattern in (a) superimposed in grey scale. (c, d) Extracts from plots similar to that in (b) and corresponding to the images of the time series captured, respectively, just before and after annihilation.

point where it is accelerated. A similar feature was observed very early for Williams rolls in N-(4-methoxybenzylidene)-4-butylaniline (MBBA) and theoretically explained using amplitude equations incorporating a gauge-field.[32] A notable feature in Fig. 7 is that the initial separation of the defect pair is about the same for different Σ_2 values and the total annihilation time is a rapidly decreasing function of Σ_2 in panels (a)-(c); but this trend breaks down in panel (d) in which Σ_2 is the largest. While Σ_2 by itself is not the factor deciding the relative velocity of defects, Δq as earlier defined has a definite bearing on the dynamics. In Fig. 9 we show that the initial uniform velocity varies linearly with Δq, which is analogous to the observation for defects in the Williams roll structure.

3.4 The metastable chevron state

In the background of the properties of edge dislocations just described, we may now consider the formation of the chevron

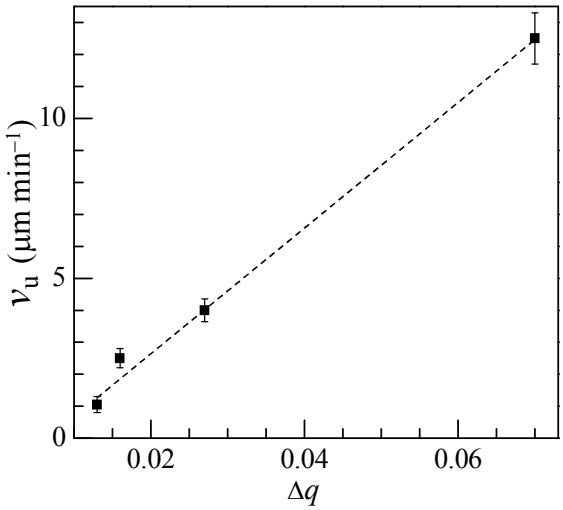

Fig. 9 Initial uniform relative velocity as a function of wave vector mismatch for a pair of opposite edge dislocations approaching each other toward annihilation; q is in units of π/d.

state. We start with the sample in the near threshold INR state and appearing optically defect-free as in Fig. 10a, and subject it to a sudden, large jump in the constraint. After a few seconds under the increased stress, a well-defined chevron texture develops as illustrated in Fig. 10b. A careful examination of the texture shows a high degree of spatial correlation in the organization of edge dislocations. The dislocations are all aligned along the y direction in parallel chains that recur at nearly the same interval along x; the topological charge is the same for all the defects in any one chain, but is opposite for the adjacent chains, as in the case of conventional dielectric chevrons. Between the defect chains, the pattern of birefringence colours is quite alike for alternate chevron bands, but varies for the adjacent bands. This is again a consequence of the inplane director deviation being of opposite sense in adjacent bands. Thus the chevron superstructure has a period λ_C equal to the separation between any two alternate defect chains.

As regards structural stability, the chevron state in 9CN differs remarkably from all the previously observed chevron states in rodlike nematics.[1-6,13-17] While the chevron superstructure shows no temporal instability in the latter case, in 9CN it relaxes systematically with efflux of time and disappears altogether in a few minutes, as indicated in Fig. 10c. The relaxation route often observed is represented by the sequence of textures in Fig. 10d-f. In the first stage of relaxation, the chevron bands alternately narrow and widen along x; simultaneously, the rolls within the narrowing bands expand and contract alternately from one roll to the next so that only the expanding rolls survive in the end; their rotational sense being the same, they merge into a single roll slightly inclined to y; in Fig. 10d, three such merged rolls are seen. In the next stage, the wave vector of the rolls within the other alternate chevron bands begins to tilt toward x, as evident from a comparison of panels (d)-(f) in Fig. 10. During this process, some of the rolls, such as the ones encircled in red in panels (e) and (f), get squeezed and disappear. In the final stage, after the wave vectors of most of the rolls are aligned along x, the sporadic unaligned rolls common to paired dislocations begin to contract, while the defect pair closes in through climb; these rolls and associated disclinations disappear relatively slowly. In effect,

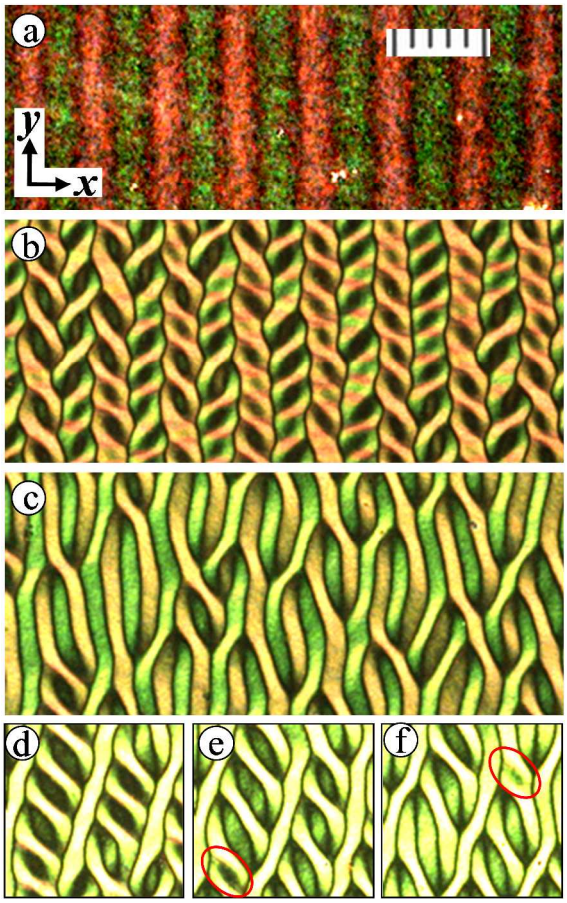

Fig. 10 Formation and relaxation of metastable chevrons in supercooled nematic 9CN. (a) Inplane normal roll state near the threshold; control parameter Σ =0.14. (b) Chevrons formed a few seconds after suddenly increasing Σ to ~28. (c) The usual edge dislocation state to which the chevron state in panel (b) has relaxed after 200 s. (d-f) Images recorded after 60, 120 and 180 s during the chevron relaxation. d=15.5 µm, f=50 kHz, T=80 °C; P(0)-A(85) in (a-c) and P(0)-A(90) in (d-f); 10 µm each scale div.

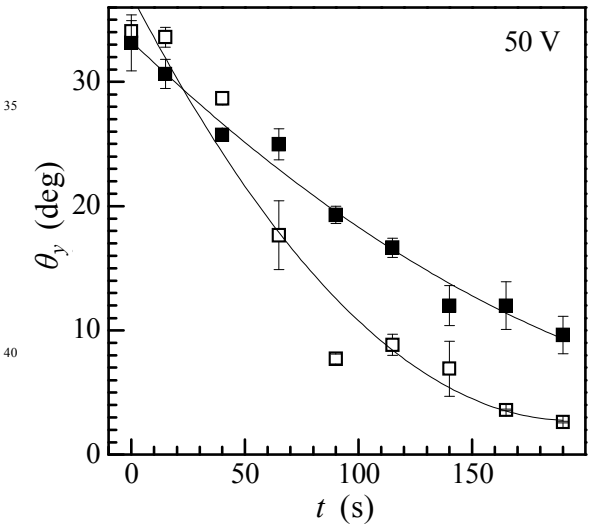

Fig. 11 Time dependence of the inclination θ_y of the line connecting paired edge dislocations with respect to the y-axis. The filled and open squares correspond to dislocation pairs from two adjacent bands of chevrons with opposite tilts. The continuous lines are parabolic fits.

the chevron relaxation process just described amounts to a reorientation of the line joining any two paired dislocations toward the normal to the easy axis. To quantify this process, we may consider the time dependence of the inclination θ_y of the line connecting paired edge dislocations with respect to the y-axis. Fig. 11 presents typical θ_y (t) plots for two defect-pairs belonging to adjacent chevron bands. The more rapidly decreasing curve corresponds to the first stage of relaxation. The flow field associated with the rolls is predominantly inplane. This is evidenced by the vortical trajectories of foreign particles suspended in the fluid. For example, in the time images (a)-(f) of Fig. 12, the encircled dust particle is seen to revolve clockwise in the layer plane, between the stagnation points, as indicated by arrows. The period of revolution is about 50 s. The overall flow field constitutes a vortex lattice as schematically presented in Fig. 12g. One may consider the relaxation of chevrons equivalently as the gradual 'melting' of this lattice.

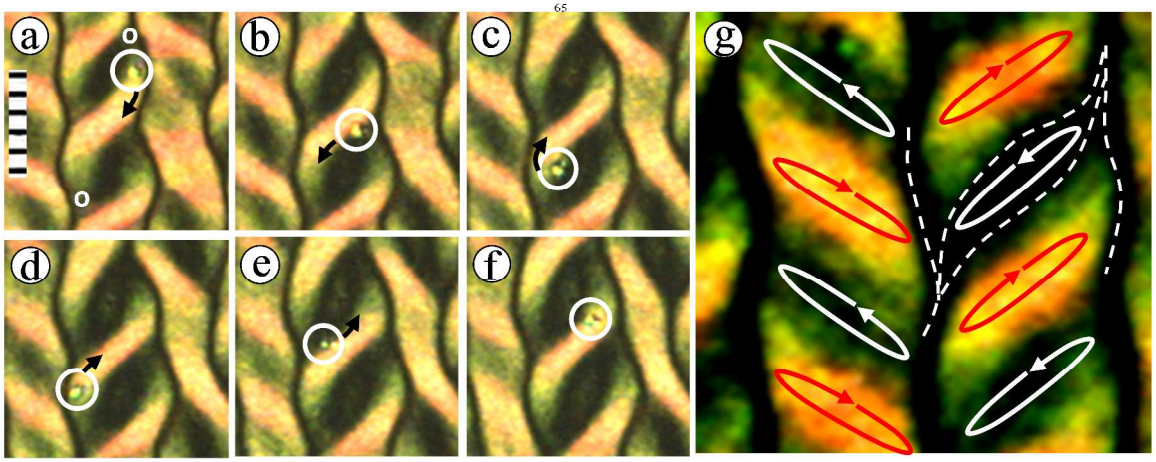

Fig. 12 Flow field within the chevrons of the INR state as revealed by tracer particle motion; in the time images (a)-(f), the encircled dust particle is seen to revolve clockwise in the layer plane, as indicated by arrows, between the stagnation points [small white circles in (a)]; successive panels are separated by 10 s. 50 kHz. 80 °C. P(0)-A(90). 5 µm each scale division. (g) Schematic representation of the vortex lattice corresponding to the chevron texture; dotted lines outline a pair of oppositely charged dislocations.

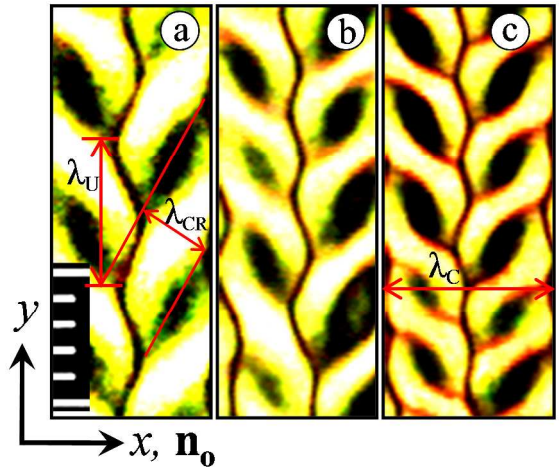

Fig. 13 Vertical undulatory dark line outlining the transition zone between bands of equal and opposite azimuthal tilts, and with the wave length λ_U a decreasing function of voltage; U= 60 V (a), 80 V (b) and 100 V (c). 50 kHz. Nearly crossed polarizers, P(0)-A(85). Images with strong enhancement of contrast and brightness. 5 µm each scale div.

Adjacent chevron bands of opposite azimuthal tilt are separated by a transitional zone within which azimuthal tilt gradually drops to zero toward the zone-centre. The central line thus appears dark between crossed polarizers P(0)-A(90). As a rule, in a well-formed chevron structure, this line is undulatory with a periodicity λ_U that determines the maximum defect density corresponding to any given voltage; λ_U is a measure of λ_{CR}, the period of chevron rolls, which is given by $\lambda_{CR}=\lambda_U \sin\theta_y$. The field variation of λ_U is illustrated by the textures in Fig. 13a-c; λ_U decreases significantly with increasing field. Apart from λ_U, the other modulation associated with the chevron state is λ_C, the period of the chevron superstructure along x. After complete relaxation of the chevrons, we find only the inplane normal rolls with a period λ_N. In Fig. 14, the periods λ_C, λ_U and λ_N measured at various voltages are plotted against Σ. λ_C, which shows a scatter in the range $(2.6\pm0.2)d$, may be taken as almost independent of Σ; by contrast, for dielectric chevrons in calamitics, $\lambda_C(\Sigma)$ is a slowly decreasing function.[10] In fact, bent-core chevrons here and dielectric chevrons have more fundamental differences. The former are metastable and form only at very large values of Σ within the already existing INR state, but the latter are stable and form from the normal rolls at voltages marginally above threshold. In other words, in bent-core chevrons, the wide domains constitute the initial state in which dislocations generate the relatively narrower secondary chevron rolls; in dielectric chevrons, the narrow rolls are primary and the wide domains separated by defect chains are secondary. Notwithstanding these differences, in terms of the mean distance between successive defects along a defect chain as a function of constraint, the two cases have a qualitative correspondence. In Fig. 14, λ_U is seen to decrease smoothly with increasing constraint between Σ=10 and Σ =65; the curve may broadly be divided into two linear segments on either side of $\Sigma\approx30$ with the slope $d\lambda_U/d\Sigma$ being greater for the lower Σ region. For dielectric chevrons, the reported[10] dependence of defect-separation Δy on Σ has similar features, with Δy decreasing linearly, at a rate faster for Σ =0.2-0.24 and slower for Σ =0.24-0.32. The fall in the rate is interpreted as on account of the crossover into the regime of fully developed chevrons.

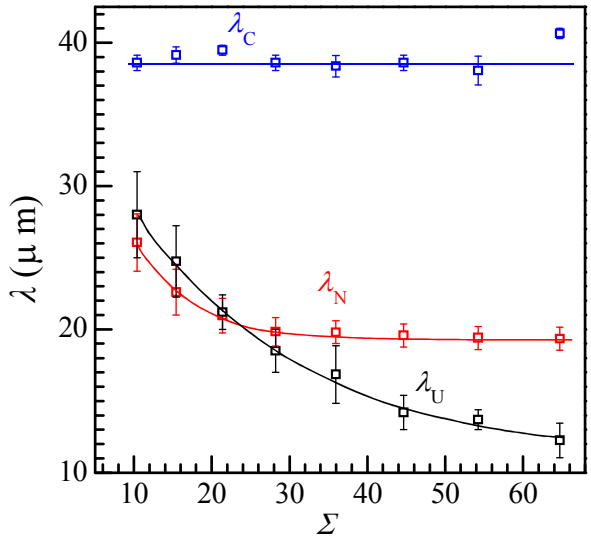

Fig. 14 Different modulations associated with the chevron and INR modes: λ_c is the period of the chevron superstructure along x prior to any significant relaxation of this structure, and λ_U is the corresponding period of the undulatory boundary between adjacent chevron bands; λ_N is the period of inplane rolls after near complete relaxation of the chevron state.

After the chevron structure relaxes, we return to the INR state with a characteristic period $\lambda_N < \lambda_C$ in the entire region of large Σ wherein the chevrons form. $\lambda_N(\Sigma)$ shows a steep initial fall, but becomes flat for large values of Σ as seen in Fig.14. This λ_N-saturation region is unstable toward the formation of disclinations which occurs in time of the order of minutes. We have characterized the disclination state in detail in our earlier reports.[21,22] Here we may note an interesting aspect of disclinations in relation to chevrons. These disclinations nucleate and grow along lines of zero distortion parallel to y, and at intervals of λ_N along x. They are undulated and, therefore, cause a similar distortion in the neighboring regions. In consequence, edge dislocations reappear in these regions as shown in Fig. 15.

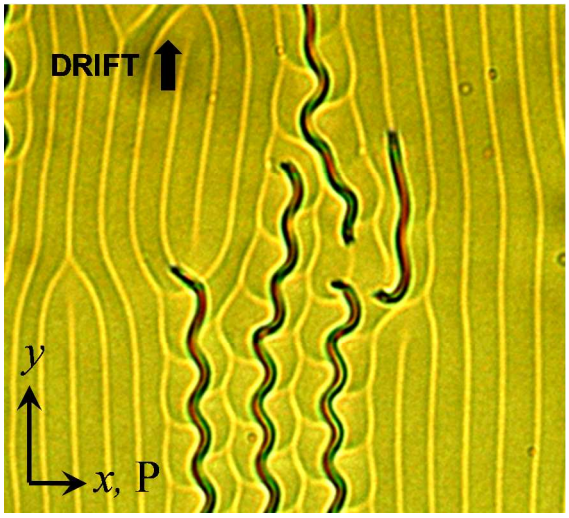

Fig. 15 Worm-like drifting disclinations in the normal roll state derived from the chevron state at Σ=36. The undulatory distortion in the neighborhood of disclinations causes edge dislocations to reform. Single polarizer along x.

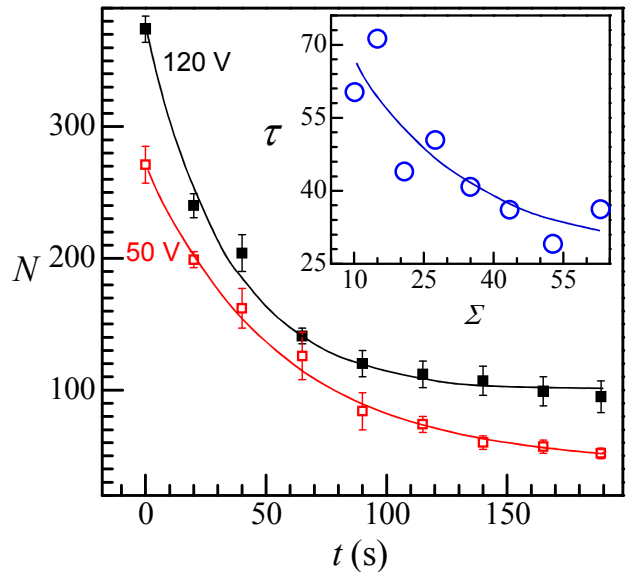

Fig. 16 The number of edge dislocations N in a 320x210 μm^2 area of the sample as a function of time. The data are from the images of relaxing chevrons captured over 200 s, with an interval of 1 s between successive images. The time t=0 corresponds to that of fully developed chevron state or maximum dislocation density obtained after a few seconds of switching U from 16 V to the voltage indicated. Inset: Relaxation time as a function of control parameter; the continuous line indicates $\tau(\Sigma)$ to be broadly an exponentially decreasing function.

Finally, we consider the dynamics of defects associated with the chevron state. From the images of relaxing chevrons captured over 200 s, with an interval of 1 s between successive images, we determined the number of edge dislocations N within an area of 320x210 μm^2 as a function of time. Fig. 16 shows the variation $N(t)$ for two voltages of chevron formation. The time t=0 corresponds to that of fully developed chevron state or maximum dislocation density obtained after a few seconds of switching U from 16 V to the voltage indicated. The continuous curves through the $N(t)$ data points are the exponential fits conforming to the decay expression

$$(N_t - N_\infty) = (N_o - N_\infty)\, e^{-t/\tau}, \qquad (2)$$

where N_o, N_t and N_∞ are the number of dislocations at times 0, t and ∞, respectively; and τ is the relaxation time reminiscent of the mean life in radioactive decay. For U=50 V, we find N_∞= 40 and τ=58.4 s; similarly, for U=120 V, N_∞= 93 and τ=42 s. The inset in Fig. 16 shows the variation of τ as a function of Σ; the continuous line therein indicates $\tau(\Sigma)$ to be broadly an exponentially decreasing function.

3.5 Significance of the observed edge dislocation dynamics

It is useful to first recall some related earlier observations for later comparison. In a typical coarsening experiment, first, the system is constrained to undergo a sudden transition, deep into a phase of symmetry lower than that of the precursor phase. Thereby, a network of topological defects is formed, bridging the multifarious incompatible domains growing at different sites. The ensuing time evolution of the defect pattern is in many cases found to be governed by universal scaling laws, encompassing fields as diverse as soft condensed matter and cosmology.[27] Liquid crystals have proved an ideal media for the study of this equilibration process because of easy visualization of defects and convenient time scales. There have been numerous theoretical,[27,42,43] experimental[44-56] and simulation[50,56-60] studies on defect dynamics in liquid crystals, particularly nematics. For systems with a continuous symmetry and nonconserved order parameter, the time-dependent Ginzburg-Landau (GL) model predicts an algebraic growth of correlation length, $\xi(t) \propto t^c$, with c=0.5.[42] This and related predictions on the interdefect separation, defect density and structure factor have been broadly verified for a variety of defect types. Principally, defects in nematics are walls bridging regions of opposite tilts, rotational director dislocations (disclinations), and monopoles (point defects or hedgehogs).[61] For electrically induced elliptical walls in free-standing nematic films, it is observed that the rate of collapse of the major axis a is inversely proportional to a.[53] This translates into a varying as $t^{0.5}$ with t as the time to collapse. In some early studies, disclination loops (closed singular lines of charge ½) have also been found[44,46,51] to collapse with their radius $r(t)$ proportional to $t^{0.5}$. On the other hand, for twist disclination loops separating untwisted and π-twisted regions, $r(t)$ is both predicted and observed to be linear in t.[54] In a dense tangle of disclinations generated by a pressure quench from the isotropic to the nematic phase, the disclination length per unit volume is found to show the ideal t^{-1} scaling.[44-46] Annihilation of radial and hyperbolic hedgehogs,[48] as also of opposite umbilical defects of unit strength,[55,56] is also found to follow the dynamic scaling laws.

We may now consider the dynamics of edge dislocations. Given a single length scale ξ, the number of dislocations per unit area ρ ought to vary as ξ^{-2}. In line with the dimensional argument for disclinations,[52] balancing the force Γ/ξ between the annihilating pair against the frictional force ηv, we have $v = \Gamma/\xi\eta$; here Γ is the energy per unit length of dislocation and η is the effective viscosity coefficient. From the dissipation principle that the rate of free energy gain stems from the corresponding energy loss due to viscous friction, we obtain $d(\rho v)/dt = \rho\eta v^2$; this leads again to $\xi(t) \propto t^{0.5}$. Such an algebraic scaling is also derived in a numerical simulation of the Newell-Whitehead equation for a pair of dislocations created through the Eckhaus instability.[60] It is explained as a consequence of the saddle-node type catastrophe and, therefore, of universal relevance. Notably it applies specifically to late-time dynamics,[34,36] since the interaction force between the defects gets augmented only within a short range of their separation. The phase diffusion model predicts the distortion to exponentially fall off in front with a length scale linear in $1/v_u$, where v_u is the uniform early-time climb rate; behind the dislocation, the decay of distortion with distance follows the power law with exponent –0.5.[34] By implication, for defect separations $s > s^* \propto 1/v_u$ the motion is uniform, and for $s < s^*$ it is accelerated and the attraction dominates the Peach-Koehler force. Our results in Fig. 7 are in broad agreement with these predictions. From the linear log-log plots of s against t in the region of acceleration, or for separations below s^*, we find the critical exponent to be generally less than 0.5. The exponent corresponding to the data for Σ=0.014 in Fig. 7a is 0.43. It is nearly the same for Σ=0.05 (Fig. 7b), but decreases to 0.34 for Σ=0.1 (Fig. 7c) and further to 0.30 for Σ=0.5 (Fig. 7d). Ideal

scaling behaviour may require the control parameter to be very close to the threshold. This is not experimentally feasible since the near-threshold pattern, which involves only inplane director deviations and requires birefringence contrast to be seen, is nearly unobservable. In fact, the optical threshold is higher than the real threshold, which is a limitation to an extent in all optical pattern studies. Secondly, a single correlation length is an approximation in anisotropic systems. This is demonstrated for the dynamics of dislocations in classical nematic electroconvection patterns;[37] the growth exponent for one principal direction is estimated as 1/3 and for the other as 1/5, instead of the expected 1/2.

Coming to early-time kinetics $s(t)$ prior to acceleration, it is governed by the deviation of the wave number from its optimum value, Δq. This is entirely as in conventional normal roll electroconvection, where, according to a theoretical description involving both GL and gauge-field equations, the uniform defect velocity v_u, either for two defects far separated or an isolated defect, should vary as Δq, regardless of the control parameter.[32] The $v_u(\Delta q)$ variation in Fig. 9 is in agreement with this prediction.

An important aspect of coarsening in convective systems concerns the role of the flow field in moderating the defect dynamics. This is theoretically examined for the motion of dislocations in the Rayleigh-Bénard roll structure.[62] It is found that the driving force is a superposition of two independent forces: The Peach-Koehler force acting to alleviate the wavevector mismatch and the advection force, originating in curvature gradients at defect sites and acting to reduce the wave number. When these forces act in conflict and are balanced, the dislocation pair remains bound and stationary. Evidently, the advection force may be expected to be quite significant for inplane flows particularly when Σ is large. But it cannot explain the lowering of the growth exponent under increasing Σ when both the forces tend to change the wave number in the same way.

The exponential decrease of dislocations as seen in Fig. 16 would seem to imply that the probability of decay of excess defects (N_t-N_∞) through annihilation, over a given incremental time, remains constant in t. This is a surprising result for a phase ordering process considering the scaling behaviour for a variety of other topological defects surveyed before. Firstly, we need to note here that the t^{-1} scaling of dislocation density is expected to hold in the asymptotic regime rather than in the early stages of coarsening. Secondly, exponential decay of defect density ρ with time is indeed to be expected under certain conditions. Pargellis et al.[43] were led to this conclusion in their combined theoretical and experimental investigation on the dynamics of wedge disclinations of unit strength generated in free-standing smectic-C films. The strain field between the defect pairs gets confined to 2π walls under interaction of topological dipoles with an ordering field E_a. Then the analysis based on the GL model leads to $\rho(t) = \rho(0)\, e^{-\mu v t}$, where t is the time since quench, μ is the cross section for intersection of the disclination with a disclination wall and v is the coalescence speed. This dependence is also supported by experimental results.[43] The origin of E_a causing the exponential decay, while not definitively identified, is conjectured to do with edge dislocations existing in the wedge shaped smectic film. For the dislocations in 9CN here a similar reasoning might apply. It is not improbable that the inplane flows around dislocations might generate a pressure field leading to an orientation ordering. If that happens, the dynamics will be affected by flow velocities and the relaxation time τ could be a function of Σ, as in the inset of Fig. 16. There are other complex factors to consider. For example, the initial chevron states for different Σ values differ in their structure; paired dislocation dipoles are aligned nearly along the easy axis for sufficiently large Σ, but they become increasingly oblique with decreasing Σ. The closer proximity of chevron defects at higher Σ values and the consequent strong overlap of distortion fields in defect pairs will influence the dynamics of stepwise degeneration of the chevron structure (Fig. 10d-f).

4 Conclusions

Edge dislocations in classical thermo- and electroconvective roll structures have earlier received considerable experimental and theoretical attention directed toward an understanding of their evolution, interaction and annihilation-dynamics. Here we have focused on dislocations arising in the nonstandard electroconvective INR state of a bent-core nematic liquid crystal, which is distinguished by a flow field composed predominantly of inlayer streamlines unlike in Rayleigh-Bénard or Williams roll structures, wherein the vortices of flow have their axes in the layer plane. Long wavelength harmonic phase variations occurring under increasing constraint are found to relax by the formation of dislocations of opposite topological charge. The steady state configuration of the system is approached through climbing motions of the defects. Annihilation is most often observed with paired defects of opposite polarity. The associated dynamics involves a uniform motion at large distances of defect-separation and accelerated motion close to annihilation. This trend is also seen in conventional roll systems, showing that the qualitative features of motion are not influenced by the nature of flow field. This result is independent of whether the imposed stress is large or small so long as the paired defects are sufficiently isolated from other defects. In the regime of relatively low control parameter, the uniform velocity varies directly as the wavevector mismatch and a scaling behaviour is seen in the late time dynamics. Unpaired opposite defects often occur in the bound state that is stable against glide. A significant realization is that the so-called knitting instability pattern, which forms on sudden application of a large field, consists of a regularly ordered arrangement of positive and negative dislocations just as in the chevron state of classical dielectric rolls. The relaxation dynamics of this state is characterized by an exponential decrease in the defect density. The characteristic relaxation time is also a function of the imposed constraint. This unusual course of phase ordering requires much further study for its proper understanding. The basic question that remains open concerns the origin and stability of the INR state itself.

Addresses

[a]*Centre for Nano and Soft Matter Sciences, P. O. Box 1329, Jalahalli, Bangalore 560 013, India; E-mail: murthyksk@gmail.com*
[b]*Raman Research Institute, C. V. Raman Avenue, Bangalore 560 080, India*

Acknowledgments

We are indebted to Prof. W. Weissflog for providing us the bent-core compound used in this study and to Prof. K. A. Suresh for his keen interest in this investigation.

References

1 L. M. Blinov and V. G. Chigrinov, *Electrooptic Effects in Liquid Crystal Materials*, Springer, Berlin, 1994.
2 S. A. Pikin, *Structural Transformations in Liquid Crystals*, Gordon and Breach Science Publishers, New York, 1991.
3 P. G. de Gennes and J. Prost, *The Physics of Liquid Crystals*, 2nd ed., Clarendon Press, Oxford, 1993.
4 Orsay Liquid Crystal Group, *Phys. Rev. Lett*., 1970, **25**, 1642.
5 Orsay Liquid Crystal Group, *Mol. Cryst. Liq. Cryst*., 1971, **12**, 251.
6 R. Ribotta and G. Durand, *J. Phys. (Paris), Colloq*. *C*3, 1979, **40**, 334.
7 L. Nasta, A. Lupu, and M. Giurgea, *Mol. Cryst. Liq. Cryst*., 1981, **71**, 65.
8 M. Scheuring, L. Kramer, and J. Peinke, *Phys. Rev. E*: *Stat., Nonlinear, Soft Matter Phys.*, 1998, **58**, 2018.
9 A. G. Rossberg and L. Kramer, *Physica D*, 1998, **115**, 19.
10 H. Amm, M. Grigutsch, and R. Stannarius, *Mol. Cryst. Liq. Cryst*., 1998, **320**, 11.
11 H. Amm, R. Stannarius, and A. G. Rossberg, *Physica D*, 1999, **126**, 171.
12 S. Komineas, H. Zhao, and L. Kramer, *Phys. Rev. E: Stat., Nonlinear, Soft Matter Phys.*, 2003, **67**, 031701.
13 A. N. Trufanov, L. M. Blinov, and M. Barnik, *Sov. Phys. JETP*, 1980, **51**, 314.
14 A. N. Trufanov, L. M. Blinov, and M. Barnik, in *Advances in Liquid Crystal Research and Applications*, edited by L. Bata, Pergamon Press, Oxford, 1980, p. 549.
15 J-H. Huh, Y. Hidaka, A. G. Rossberg, and S. Kai, *Phys. Rev. E*: *Stat., Nonlinear, Soft Matter Phys.*, 2000, **61**, 2769.
16 J-H. Huh, Y. Hidaka, and S. Kai, *Mol. Cryst. Liq. Cryst*., 2001, **366**, 833.
17 J-H. Huh, Y. Yusuf, Y. Hidaka, and S. Kai, *Phys. Rev. E*: *Stat., Nonlinear, Soft Matter Phys.*, 2002, **66**, 031705.
18 M. Petrov, E. Keskinova, and B. Katranchev, *J. Mol. Liq*., 2008, **138**, 130.
19 D. Wiant, J. T. Gleeson, N. Éber, K. Fodor-Csorba, A. Jakli, and T. Toth-Katona, *Phys. Rev. E*: *Stat., Nonlinear, Soft Matter Phys.*, 2005, **72**, 041712.
20 S. Tanaka, S. Dhara, B. K. Sadashiva, Y. Shimbo, Y. Takanishi, F. Araoka, K. Ishikawa, and H. Takezoe, *Phys. Rev. E*: *Stat., Nonlinear, Soft Matter Phys.*, 2008, **77**, 041708.
21 P. Tadapatri, U. S. Hiremath, C. V. Yelamaggad, and K. S. Krishnamurthy, J. Phys. Chem. B, 2010, **114**, 10.
22 P. Tadapatri, K. S. Krishnamurthy, and W. Weissflog, *Phys. Rev. E*: *Stat., Nonlinear, Soft Matter Phys.*,. 2010, **82**, 031706.
23 P. Tadapatri and K. S. Krishnamurthy, *J. Phys. Chem. B*, 2012, **116**, 782.
24 S. Kaur, A. Belaissaoui, J. W. Goodby, V. Görtz, and H. F. Gleeson, *Phys. Rev. E*: *Stat., Nonlinear, Soft Matter Phys.*, 2011, **83**, 041704.
25 Y. Xiang, Yi-Kun Liu, Á. Buka, N. Éber, Zhi-Yong Zhang, Ming-Ya Xu and E. Wang, *Phys. Rev. E*: *Stat., Nonlinear, Soft Matter Phys.*,. 2014, **89**, 012502.
26 P. Kumar, U. S. Hiremath, C. V. Yelamaggad, A. G. Rossberg, and K. S. Krishnamurthy, *J. Phys. Chem. B*., 2008, **112**, 9270.
27 A. J. Bray, *Adv. Phys*., 1994, **43**, 357
28 E. Guazelli, E. Guyon, and J. E. Wesfreid, *Phil. Mag. A*, 1983, **48**, 709.
29 E. Dubois-Violette, E. Guazzelli, and J. Prost, *Phil. Mag. A*, 1983, **48**, 727.
30 R. Ribotta and A. Joets, in *Cellular Structures in Instabilities*, edited by J. E. Wesfreid and S. Zaleski, Springer-Verlag, New York, 1984, p. 249.
31 E. Bodenschatz, W. Pesch, and L. Kramer, *Physica D*, 1988, **32**, 135.
32 G. Goren, I. Procaccia, S. Rasenat, and V. Steinberg, *Phys. Rev. Lett*., 1989, **63**, 1237.
33 S. Rasenat, V. Steinberg, and I. Rehberg, *Phys. Rev. A*: *Atomic, Molecular and Optical Phys*., 1990, **42**, 5998.
34 E. Bodenschatz, A. Weber, and L. Kramer, *J. Stat. Phys.*, 1991, **64**, 1007.
35 E. Braun and V. Steinberg, *Europhys. Lett*., 1991, **15**, 167.
36 S. Kai, Y. Hidaka, K. Hayashi, and M. I. Tribelsky, *J. Phys. Soc. Jpn*., 1996, **65**, 3419.
37 C. Kamaga, F. Ibrahim, and M. Dennin, *Phys. Rev. E*: *Stat., Nonlinear, Soft Matter Phys.*, 2004, **69**, 066213.
38 L. Purvis and M. Dennin, *Phys. Rev. Lett*., 2001, **86**, 5898.
39 S. Chandrasekhar and G. S. Ranganath, *Adv. Phys.*, 1986, **35**, 507.
40 D. Johnson and A. Saupe, *Phys. Rev. A*: *Atomic, Molecular and Optical Phys.*, 1977, **15**, 2079.
41T. E. Oliphant, *Comput. Sci. Eng*. 2007, **9**, 10.
42 R. A. Wickham, *Phys. Rev. E*: *Stat., Nonlinear, Soft Matter Phys.*, 1997, **56**, 6843.
43 A. N. Pargellis, P. Finn, J. W. Goodby, P. Penizza, B. Yurke, and P. E. Cladis, *Phys. Rev. A*: *Atomic, Molecular and Optical Phys*., 1992, **46**, 7765.
44 I. Chuang, N. Turok, and B. Yurke, *Phys. Rev. Lett.*, 1991, **66**, 2472.
45 I. Chuang, R. Durrer, N. Turok, and B. Yurke, *Science*, 1991, **251**, 1336.
46 I. Chuang, B. Yurke, and A. N. Pargellis, *Phys. Rev. E*: *Stat., Nonlinear, Soft Matter Phys.*, 1993, **47**, 3343.
47 N. Mason, A. N. Pargellis, and B. Yurke, *Phys. Rev. Lett.*, 1993, **70**, 190.
48 A. N. Pargellis, J. Mendez, M. Srinivasarao, and B. Yurke, *Phys. Rev. E: Stat., Nonlinear, Soft Matter Phys.,*1996, **53**, 25(R).
49 B. Yurke, A. N. Pargellis, S. N. Majumdar, and C. Sire, *Phys. Rev. E: Stat., Nonlinear, Soft Matter Phys.,*1997, **56**, 40(R).
50 K. Minoura, Y. Kimura, K. Ito, R. Hayakawa, *Mol. Cryst. Liq. Cryst*., 1997, **302**, 345.
51 W. Wang, T. Shiwaku, and T. Hashimoto, *J. Chem. Phys.*, 1998, **108**, 1618.
52 F. Elias, S. M. Clarke, R. Peck, and E. M. Terentjev, *Europhys. Lett*., 1999, **47**, 442.
53 P. Tadapatri and K. S. Krishnamurthy, *J. Phys. Chem. B*, 2008, **112**, 13509.
54 P. Tadapatri and K. S. Krishnamurthy, *Soft Matter*, 2011, 7, 6273.
55 I. Dierking, O. Marshall, J. Wright, and N. Bulleid, *Phys. Rev. E*: *Stat., Nonlinear, Soft Matter Phys.*, 2005, **71**, 061709.
56 I. Dierking, M. Ravnik, E. Lark, J. Healey, G. P. Alexander and J. M. Yeomans, *Phys. Rev. E*: *Stat., Nonlinear, Soft Matter Phys.*, 2012, **85**, 021703.
57 J. L. Billeter, A. M. Smondyrev, G. B. Loriot, and R. A. Pelcovitis, *Phys. Rev. E*: *Stat., Nonlinear, Soft Matter Phys.,*1999, **60**, 6831.
58 R. A. Pelcovits, J. L. Billeter, A. M. Smondyrev, and G. B. Loriot, in *Defects in Liquid Crystals: Computer Simulations, Theory and Experiments*, edited by O. D. Lavrentovich, P. Pasini, C. Zannoni and S. Žumer, Kluwer Academic Publishers, Dordrecht, 2001, p. 141.
59 B. F. de Oliveira, P. P. Avelino, F. Moraes, and J. C. R. E. Oliveira, *Phys. Rev. E*: *Stat., Nonlinear, Soft Matter Phys.,*2010, **84**, 041707.
60 H. Sakaguchi, *Prog. Theor. Phys*., 1991, **85**, 927.
61 M. Kleman, *Points, Lines and Walls*, John Wiley & Sons, Chichester, 1983.
62 Th. Walter, W. Pesch, and E. Bodenshatz, *Chaos*, 2004, **14**, 933.